Comparison of Pericardium Modeling Approaches for Mechanical Whole Heart Simulations

Jonathan Krauß, Tobias Gerach, Axel Loewe

Institute of Biomedical Engineering, Karlsruhe Institute of Technology (KIT), Karlsruhe, Germany

Abstract

The restraining effect of the pericardium and surrounding tissues on the human heart is essential to reproduce physiological valve plane movement in simulations and can be modeled in different ways. In this study, we investigate five different approaches used in recent publications and apply them to the same whole heart geometry. Some approaches use Robin boundary conditions, others use a volumetric representation of the pericardium and solve a contact problem. These two strategies are combined with a smooth spatially varying scaling or a region-wise partitioning of the epicardial surface. In general, all simulations follow the same morphology regarding mitral valve displacement, tricuspid valve displacement and left ventricular twist. We show that – with the parameters used in the original papers – Robin boundary conditions are computationally more expensive and lead to smaller stroke volumes and less ventricular twist. Unrelated to this, simulations with a penalty scaling result in a less pronounced displacement of the tricuspid valve. In one of the investigated scenarios adipose tissue is modeled using a volumetric mesh and the Robin boundary conditions are applied on its outside surface. We conclude that this approach leads to similar results as a partitioning of the epicardial surface into two regions with different penalty parameters and therefore a volumetric representation of the adipose tissue is neither necessary nor practical.

1. Introduction

The human heart sits inside the thoracic cavity and is enclosed in the pericardial sac (or pericardium). The pericardium restricts cardiac motion during the heart cycle [1]. This is accounted for in mechanical cardiac modeling with different approaches. Fritz et al. [2] modeled the pericardium as an elastic body in contact with the epicardium. A bidirectional penalty formulation allows the heart to slide along the pericardial surface without friction. Pfaller et al. [3] filled the space between the epicardial surface and the pericardium with adipose tissue and simplified the aforementioned approach by replacing the pericardium with Robin boundary conditions using a spring-dashpot formulation with constant spring stiffness and damping coefficient. Strocchi et al. [4] used similar boundary conditions but with a spatially varying penalty scale factor that is derived from cardiac motion seen in magnetic resonance imaging (MRI) cine data. Fedele et al. [5] partitioned the epicardial surface in regions with constant spring stiffnesses. The regions in contact with the pericardium are more restricted than the regions in contact with epicardial adipose tissue (EAT). The aim of this paper is to provide a quantitative comparison between these approaches.

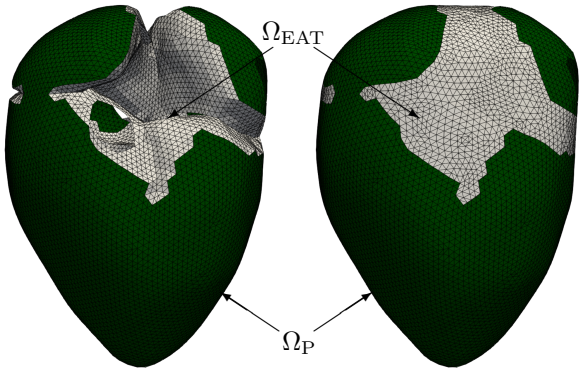

Figure 1. Partitioning of contact surface in two regions Ω_{P} (green) and Ω_{EAT} (grey) with varying boundary conditions. Left: Ω_{EAT} defined on the epicardium. Right: Ω_{EAT} defined on the outside of adipose tissue (scenario 3).

2. Methods

All simulations were conducted on a whole heart geometry derived from single patient MRI data [6]. We used rule-based methods to generate the fiber orientations on the atria [7] and the ventricles [8, 9] with epicardial and endocardial ventricular fiber angles of -41° and 66°, respectively [10]. Local activation times were precomputed using the monodomain equation on an undeformed mesh (control setup in [6]). Based on these activation times, contractile forces were generated using a phenomenological active tension model [11] and applied via an active stress approach. The passive mechanical behavior of both atria and ventricles was modeled us-

ing the orthotropic material model by Usyk et al. [12]. Valves and blood vessels – as well as pericardium and adipose tissue (if volumetric representations existed) – were modeled using an isotropic Neo-Hookean material [6] with $\mu_{\text{Valves}} = 1\,\text{MPa}$, $\mu_{\text{Vessels}} = 7.45\,\text{kPa}$, $\mu_{\text{Peri}} = 2\,\text{kPa}$, $\mu_{\text{EAT}} = 3.73\,\text{kPa}$, $\kappa_{\text{EAT}} = 1\,\text{kPa}$ and $\kappa_{\text{Valves}} = \kappa_{\text{Vessels}} = \kappa_{\text{Peri}} = 650\,\text{kPa}$. The circulatory system is represented by a closed-loop lumped parameter model [13]. To approximate the pressure-free reference configuration and fit the passive mechanical properties, we used an iterative algorithm developed by Marx et al. [14]. For both atria and ventricles they are $\mu = 34.64\,\text{Pa}$, $b_{ff} = 32.8$, $b_{ss} = b_{nn} = b_{ns} = 13.12$, $b_{fs} = b_{fn} = 22.96$ and $\kappa = 6.5 \times 10^5\,\text{Pa}$ in accordance with the nomenclature used by Gerach et al. [6]. All other simulation parameters were set as in [6].

The focus of this paper is on the different approaches of modeling the interaction between the human heart and the pericardium. While the veins are fixated in all directions and the arteries are restricted with Robin boundary conditions for all simulation scenarios, the restriction of the epicardial surface depends on the chosen simulation scenario. In general, all scenarios follow a simple rule such that the stress $\boldsymbol{P}_{\text{E}}$ acting on the epicardial surface is computed based on the normal $\boldsymbol{N}$, the distance to the pericardium d_{EP}, its time derivative, a stiffness or penalty parameter $k_\perp$ and a damping coefficient $c_\perp$:

$$\boldsymbol{P}_{\text{E}} = \left(k_\perp d_{\text{EP}} + c_\perp \frac{\partial d_{\text{EP}}}{\partial t} \right) \boldsymbol{N} \otimes \boldsymbol{N} = p_{\text{EP}} \boldsymbol{N} \otimes \boldsymbol{N} \quad (1)$$

In scenarios where a volumetric mesh is used for the pericardium and a contact problem is solved, the partner element in the pericardium is updated in each time step and the distance d_{EP} is calculated using the current normal $\boldsymbol{n}$ and the current locations of the epicardial surface element ($\boldsymbol{x}_{\text{E}}$) and the updated pericardial element ($\boldsymbol{x}_{\text{P}}$): $d_{\text{EP}} = (\boldsymbol{x}_{\text{P}} - \boldsymbol{x}_{\text{E}}) \cdot \boldsymbol{n}$. This is not the case for the scenarios using Robin boundary conditions [3–5]. Here, d_{EP} is computed using the initial surface normal $\boldsymbol{n}_0$ and the initial position $\boldsymbol{x}_{\text{E},0}$ of the element: $d_{\text{EP}} = (\boldsymbol{x}_{\text{E},0} - \boldsymbol{x}_{\text{E}}) \cdot \boldsymbol{n}_0$.

We partitioned the epicardial surface in two regions as shown in Figure 1 based on whether the elements are in contact with the pericardium (Ω_{P}) or not (Ω_{EAT}). In addition, we calculated a spatially varying scaling coefficient similar to [4] as pictured in Figure 2. Based on this, five different scenarios were considered:

Scenario 1: Sliding contact formulation according to Fritz et al. [2] with constant contact penalty $k_\perp = 5 \times 10^7\,\text{Pa}\,\text{m}^{-1}$ and a volumetric mesh for the pericardium in contact with Ω_{P} (see Figure 1).

Scenario 2: Sliding contact formulation [2] from scenario 1 with added penalty scaling according to Figure 2.

Scenario 3: Robin boundary conditions on Ω_{P} and the outer surface of volumetric adipose tissue which fills the space between Ω_{EAT} (Figure 1, right) and the pericardium with constant $k_\perp = 2 \times 10^5\,\text{Pa}\,\text{m}^{-1}$ and $c_\perp = 5 \times 10^3\,\text{Pa}\,\text{s}\,\text{m}^{-1}$ [3].

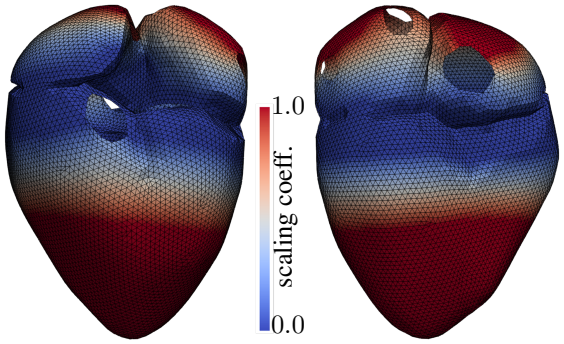

Figure 2. Spatially varying penalty scaling coefficient ranging from 0 to 1 visualized on the epicardial surface. Left: Anterior view, right: Posterior view.

Scenario 4: Robin boundary conditions on both Ω_{P} and Ω_{EAT} scaled according to Figure 2 with a maximum stiffness of $k_{\perp,\text{max}} = 1 \times 10^7\,\text{Pa}\,\text{m}^{-1}$ [4].

Scenario 5: Robin boundary conditions with constant $k_{\perp,\text{P}} = 2 \times 10^5\,\text{Pa}\,\text{m}^{-1}$, $c_{\perp,\text{P}} = 2 \times 10^3\,\text{Pa}\,\text{s}\,\text{m}^{-1}$ on Ω_{P} and $k_{\perp,\text{EAT}} = 2 \times 10^2\,\text{Pa}\,\text{m}^{-1}$, $c_{\perp,\text{EAT}} = 2\,\text{Pa}\,\text{s}\,\text{m}^{-1}$ for Ω_{EAT} [5].

For all approaches, we investigated the resulting LV twist angle θ, as well as the mitral valve displacement (MVD) and the tricuspid valve displacement (TVD) time series, which we compared to measured MRI data from the same subject. Additionally, we compared the maximum of the mean contact pressures and contact distances for Ω_{P} and Ω_{EAT}.

3. Results

Time series of the MVD, the TVD and the LV twist angle θ are shown in Figure 3. For the mitral valve, the displacement in apicobasal direction is similar for all simulations and all of them are in good agreement with the measured MRI data. The approaches using penalty scaling show slightly less movement of the mitral valve during the ventricular contraction. Larger differences between the investigated approaches can be seen for the displacement of the tricuspid valve. While all simulations follow the MRI TVD morphology with an initial positive displacement phase caused by atrial contraction followed by a larger negative displacement resulting from ventricular contraction, the magnitudes of displacement differ. The original Fritz et al. [2] sliding contact formulation allows for the largest TVD with a peak-to-peak ΔTVD of $23.08\,\text{mm}$ compared to $24.97\,\text{mm}$ for the MRI data. The tricuspid valve moves the least for the Robin boundary condition formulation based on Strocchi et al [4]. Here, both phases are not as pronounced as in the measured MRI

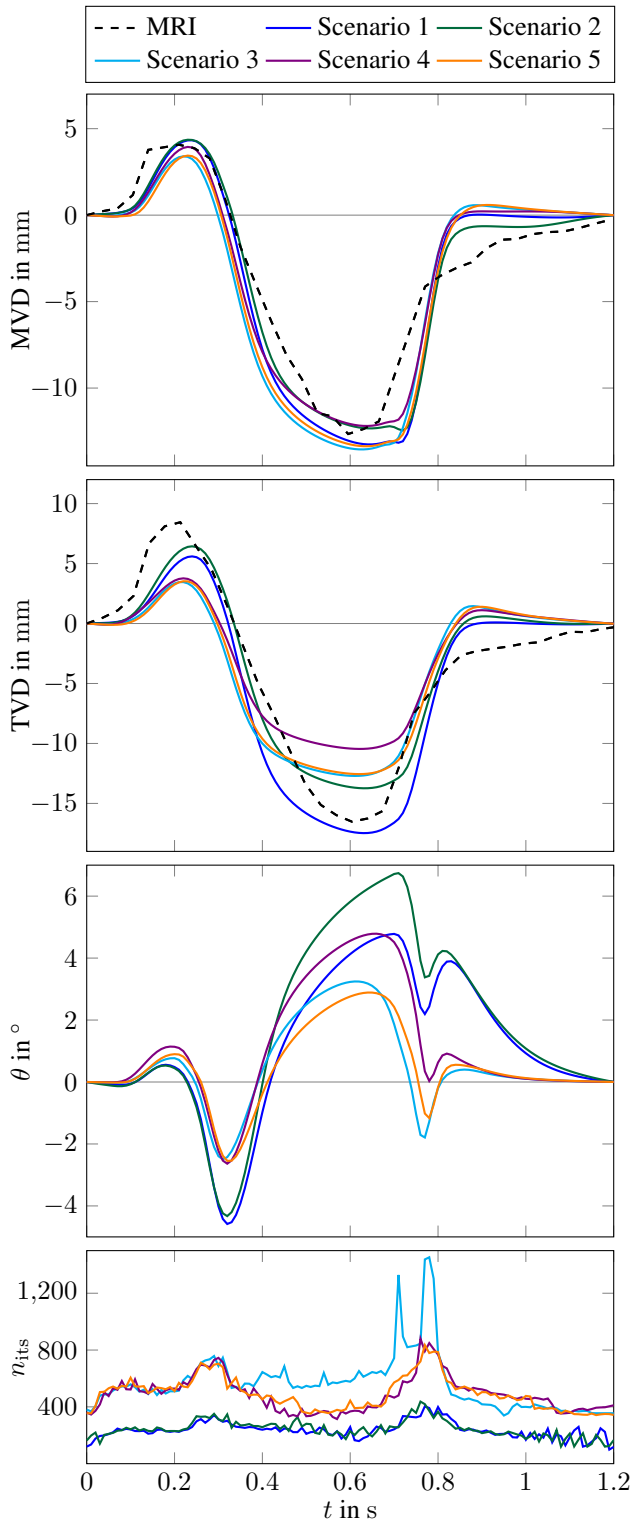

Figure 3. Mitral valve displacement (MVD), tricuspid valve displacement (TVD), LV twist angle θ and the number of iterations per export time step n_{its} for the last heartbeat of all five simulation scenarios. MVD and TVD are plotted next to measured MRI data.

Table 1. Stroke volume SV, temporal maximum of spatial mean contact pressure and mean contact distance on Ω_{P} and Ω_{EAT}: $\bar{p}^{\Omega_{\text{P}}}_{\text{max}}$, $\bar{p}^{\Omega_{\text{EAT}}}_{\text{max}}$, $\bar{d}^{\Omega_{\text{P}}}_{\text{max}}$, $\bar{d}^{\Omega_{\text{EAT}}}_{\text{max}}$ as well as the simulation time per heartbeat $\Delta t^{\text{hb}}_{\text{sim}}$ for each investigated scenario.

Scenario	SV (mL)	$\bar{p}^{\Omega_{\text{P}}}_{\text{max}}$ (kPa)	$\bar{p}^{\Omega_{\text{EAT}}}_{\text{max}}$ (kPa)
Scen. 1	114.8	17.29	-
Scen. 2	121.78	12.56	-
Scen. 3	89.7	14.08	4.82
Scen. 4	95.61	11.01	4.47
Scen. 5	88.7	14.66	0.20
	$\bar{d}^{\Omega_{\text{P}}}_{\text{max}}$ (mm)	$\bar{d}^{\Omega_{\text{EAT}}}_{\text{max}}$ (mm)	$\Delta t^{\text{hb}}_{\text{sim}}$ (min)
Scen. 1	0.57	-	46.35
Scen. 2	1.73	-	42.6
Scen. 3	0.42	0.14	189.23
Scen. 4	1.57	4.64	171.75
Scen. 5	0.44	5.92	177

data or other simulations. The corresponding peak-to-peak ΔTVD is 14.22 mm.The twist of the left ventricle – calculated as the difference in basal and apical rotation – follows a similar morphology for the five analyzed approaches. Maximum twist is generated in the sliding contact formulation with additional penalty scaling . The approaches with Robin boundary conditions show less prominent twist with the partitioned approach leading to a peak-to-peak net LV twist angle $\Delta\theta$ of 5.44° compared to 11.07° with the aforementioned approach.

Numerical results are given in Table 1. In general, approaches using Robin boundary conditions led to smaller stroke volumes than the ones with a sliding contact formulation. They also required more time for the simulation of the same number of heartbeats. Each simulation was run on a supercomputer using 24 processes on a 2.1 GHz *Intel Xeon Gold 6230* processor. Maximum mean contact pressure on Ω_{P} was between 11.01 and 17.29 kPa. In all scenarios, the resulting mean contact distance on Ω_{P} was below 2 mm. However, approaches with added penalty scaling led to increased mean contact distances compared to other scenarios. For Ω_{EAT}, there are no results available for scenarios 1 and 2 since they do not impose any restrictions there. Scenario 3 and 4 show similar maximum mean contact pressures while scenarios 4 and 5 resulted in comparable maximum mean distances.

4. Discussion

We investigated five different approaches to model the pericardium using partitioned surfaces or a smooth spatially varying penalty scaling in combination with a sliding contact or Robin boundary conditions. The corresponding parameters were taken from the papers that proposed said approaches [2–5]. For simulations in which penalty scal-

ing was applied, the regions close to the atrio-ventricular plane moved inwards and away from the pericardium. This is a direct result of the local penalty scaling being 0 and therefore no restrictions being set for the epicardial surface at these locations. This in turn led to a less pronounced TVD as can be seen in Figure 3.

Similarities between scenario 3 with a volumetric representation of adipose tissue and scenario 5 with different Robin boundary condition parameters for Ω_{EAT} can be seen in almost all results. Thus, we conclude that the restraining effect of the epicardial adipose tissue can be replaced with Robin boundary conditions to save computational time and effort and still behave similarly. The discrepancy in mean maximum contact distance on Ω_{EAT} (Table 1) is explained by the fact that for scenario 3, Ω_{EAT} is defined on the outside of the adipose tissue (see Figure 1). Thus, the epicardium is allowed to move by deforming the adipose tissue while still keeping small contact distances on Ω_{EAT}. To achieve this behavior, we decided to take the material properties of adipose tissue from [13]. With the parameters listed in the original paper [3], the adipose tissue was more incompressible which led to oscillations due to locking effects during large deformations. In general, the left ventricle twists less with Robin boundary conditions. The reason for this is that Robin boundary conditions neglect any change in normal direction and use the initial position of the element instead of a continuously updated pericardial partner element to calculate the resulting contact distance. Therefore, they are only valid for small rotations of the epicardium [3]. Considering that LV rotation is measured at up to 20° in healthy subjects [15], this is not the case. As a result, the more the current normal deviates from the reference normal, the higher the penalty of the Robin boundary conditions will be. Further investigation is warranted into why the computational times for the approaches using Robin boundary conditions are that much higher than the ones with the sliding contact formulation. One might assume that they should rather be faster because no volumetric representation of the pericardium is required and there is no need to search for new partner elements at each time step. Instead, the respective simulation times are more than three times as high because the nonlinear Newton linesearch algorithm needs more iterations to converge (on average 246 vs. 528 iterations per export time step). In conclusion, the sliding contact formulation appears to be advantageous in both computational cost and accuracy.

Acknowledgments

This research was funded by the Deutsche Forschungsgemeinschaft (DFG, German Research Foundation) – Project-ID 258734477 – SFB 1173 and LO 2093/6-1 (SPP 2311). The authors acknowledge support by the state of Baden-Württemberg through bwHPC.

References

[1] Shabetai R, et al. The pericardium and cardiac function. Prog Cardiovasc Dis 1 1979;22(2).

[2] Fritz T, et al. Simulation of the contraction of the ventricles in a human heart model including atria and pericardium : Finite element analysis of a frictionless contact problem. Biomech Model Mechanobiol 1 2014;13(3):627–641.

[3] Pfaller MR, et al. The importance of the pericardium for cardiac biomechanics: from physiology to computational modeling. Biomech Model Mechanobiol 12 2018;503–529.

[4] Strocchi M, et al. The effect of ventricular myofibre orientation on atrial dynamics. Lect Notes Comput Sc 1 2021; 12738:659–670.

[5] Fedele M, et al. A comprehensive and biophysically detailed computational model of the whole human heart electromechanics. Comput Method Appl M 5 2023; 410:115983.

[6] Gerach T, et al. The impact of standard ablation strategies for atrial fibrillation on cardiovascular performance in a four-chamber heart model. Cardiovasc Eng Technol 2023; 1–19.

[7] Wachter A, et al. Mesh structure-independent modeling of patient-specific atrial fiber orientation. CDBME 1 2015; 1(1):409–412.

[8] Schuler S. KIT-IBT/LDRB_Fibers, October 2021. URL `https://doi.org/10.5281/zenodo.4606575`.

[9] Bayer JD, et al. A novel rule-based algorithm for assigning myocardial fiber orientation to computational heart models. Ann Biomed Eng 1 2012;40(10):2243–2254.

[10] Lombaert H, et al. Human atlas of the cardiac fiber architecture: Study on a healthy population. IEEE Transactions on Medical Imaging 2012;31(7):1436–1447.

[11] Niederer SA, et al. Length-dependent tension in the failing heart and the efficacy of cardiac resynchronization therapy. Cardiovasc Res 2 2011;89(2):336–43.

[12] Usyk TP, et al. Effect of laminar orthotropic myofiber architecture on regional stress and strain in the canine left ventricle. J Elasticity 1 2000;61(1-3):143–165.

[13] Gerach T, et al. Electro-mechanical whole-heart digital twins: A fully coupled multi-physics approach. Mathematics 1 2021;9(11):1247.

[14] Marx L, et al. Robust and efficient fixed-point algorithm for the inverse elastostatic problem to identify myocardial passive material parameters and the unloaded reference configuration. J Comput Phys 2022;463:111266.

[15] Kim HK, et al. Assessment of left ventricular rotation and torsion with two-dimensional speckle tracking echocardiography. JASE 2007;20(1):45–53.

Address for correspondence:

Jonathan Krauß
Institute of Biomedical Engineering, Karlsruhe Institute of Technology (KIT), Kaiserstr. 12, 76131, Karlsruhe, Germany.
publications@ibt.kit.edu